Direct sulfation of a Zr-based Metal-Organic Framework to attain strong acid catalysts

José M. Fernández-Morales [1], Luis A. Lozano [2], Eva Castillejos-López [1], I. Rodríguez-Ramos [3], A. Guerrero-Ruiz [1], Juan M. Zamaro [1,3]

[1] Dpto. Química Inorgánica y Técnica, Facultad de Ciencias UNED, Senda del Rey 9, 28040 Madrid, Spain.

[2] Instituto de Investigaciones en Catálisis y Petroquímica, INCAPE (FIQ, UNL, CONICET). Santiago del Estero 2829 (3000), Santa Fe, Argentina.

[3] Instituto de Catálisis y Petroleoquímica, CSIC, Marie Curie 2, 28049 Madrid, Spain.

*contact author information:

E-mail: zamaro@fiq.unl.edu.ar

Full postal address: Santiago del Estero 2829 (3000) Santa Fe, Argentina

Phone and fax numbers: +55-0342-4536861.

Abstract

The application of Metal–Organic Frameworks (MOFs) in gas phase heterogeneous catalysis is still not widely spread because of their limited stability under reaction conditions. Obtaining stable acidic MOFs to be used in reactions that demand strong acid sites remains a challenge up to the present time. In this work, it is shown that nanocrystals of Zirconium MOF UiO–66 can be conveniently and easily functionalized through a simple one–pot synthetic approach, i.e. the direct treatment of UiO–66 with ammonium sulfate followed by an adequate thermal treatment, giving rise to a highly acidic and thermally stable material (named as S–UiO–66). This material can act as catalyst in the gas phase isobutene dimerization demonstrating high catalytic activity at moderate temperatures while maintaining the structural integrity of the MOF after several catalytic evaluations and/or after reuse cycles. The S–UiO–66 material represents a novel alternative in the search of robust MOF–based catalysts to be applied in gas phase heterogeneous catalytic reactions that demand strong acid sites.

Keywords: Zirconium–MOF; UiO–66; sulfate functions; acidity; isobutene dimerization

1. Introduction

The chemical and structural versatility of Metal–Organic Frameworks (MOFs) has made possible their expansion to numerous fields of applied research such as gas adsorption and storage, gas separation, biomedicine, drug release, removal of metal ions, sensor and catalysis, among others [1–7]. At the same time, several studies have been published regarding their post–synthetic functionalization which, in the field of catalysis, can extend their applicability to a greater variety of processes [7–9]. However, MOFs in gas phase heterogeneous catalysis have not been so widely employed, mainly due to their intrinsic limitations of physicochemical stability in reaction atmospheres at high temperatures and because they need appropriate functionalization in order to incorporate superficial active sites. Some examples of the use of MOFs in heterogeneous catalysis include their application in the Knoevenagel reaction, glucose transformation, xylose dehydration, or polymerizations [10–13]. However, in most cases, they are used in batch reactors and/or at low temperatures, where the thermal stability of the functionalized MOFs is not compromised. On the other hand, some reactions demand strong acid surface sites, such as alkene oligomerization, dehydrations, etc. [14]. Many commercial acidic solid acids are able to accomplish alkene oligomerization reactions, such as zeolite materials or sulfonated polystyrene resins, but for the former group the catalyst deactivation by coke formation is dominant and for the latter, their low thermal stability gives place to a destruction of the solid structures under real reaction conditions.

In recent years, some efforts have been made to obtain MOFs with high acidity, mainly through sulfonation processes by two approaches. Firstly, by the direct synthesis of MOFs employing ligands containing acid groups or functionalities able to generate acid groups, and secondly through the modification of the ligand in the MOF structure

by post–synthetic treatments. By applying the first methodology, mixed–linker metal–organic frameworks were synthesized using 5–sulfo isophthalic acid monolithium salt (m–H_2BDC–SO_3Li) and employed in the gas–phase dehydration of ethanol [15]. Similarly, UiO–66–SO_3H was obtained using monosodium 2–sulfoterephthalate as linker and employed in the acid–catalyzed Friedel–Crafts acylation of p–xylene [16]. Other sulfonated MOFs obtained by direct synthesis were reported to involve mixtures of 2–$NaSO_3$–H_2BDC and H_2BDC as starting ligands [17] and also 2–aminoterephthalic acid to obtain Zr–BDC–NH_2–SO_4 [18, 19], which were employed in adsorption applications.

Concerning MOFs acidified by post–synthetic methods a pioneering work [20] should be highlighted, in which the ligands of MIL–101(Cr) and MIL–53(Al) were sulfonated employing sulfuric acid with trifluoromethanesulfonic anhydride in nitromethane, followed by a deep washing process. Another variant was the synthesis of a thiol–laced UiO–66–type framework then post–synthetically oxidized to obtain UiO–66$(SO_3H)_2$ with the sulfonic acid groups covalently linked to the backbone of the system and tested in proton conductivity applications [21]. Similarly noteworthy was the post–synthetic preparation of the sulfated–derived MOF–808 [22] and the analogue Hf–based MOF VNU–11–SO_4 [23] employing long treatments with aqueous sulfuric acid, followed by solvent exchanges with anhydrous acetone and chloroform and then evacuated at elevated temperature. In another variant, the sulfonic acid–functionalized MOFs MIL–101(Cr)–SO_3H, UiO–66(Zr)–SO_3H and MIL–53(Al)–SO_3H were obtained by a post–synthetic modification of the linkers through treatments with chlorosulfonic acid at 0 °C in CH_2Cl_2 [24, 25]. All the sulfone–derived MOFs obtained by the aforementioned post–synthetic methods were evaluated in standard liquid phase catalytic test reactions of moderate acid demand that included esterification reactions [21, 26], citronellal cyclization and alpha–pinene isomerization [22], synthesis of

benzoxazoles [23], synthesis of quinazolinones and benzimidazoles [27], fructose dehydration to 5–hydroxymethylfurfural [24] and hydrolysis of an acetal [25], respectively. Notice that practically none of these reactions were performed in a continuous flow gas phase reactor and that in most of the preparation methods the increase in acidity of the MOFs was associated with modifications in the organic component of the materials, mainly introducing sulfonic functions. Furthermore, many of these modified MOFs lacked stability to be applied in reactions catalyzed by acids which required temperatures above 200 °C. Very recently, using the solid described in reference 22, a remarkable performance in a heterogeneous catalytic application was reported [28]. These materials demonstrated to be active, selective and stable in the low temperature dimerization of isobutene, but the presence of water was compulsory to achieve the catalytic properties. Therefore, a catalytic reaction mechanism similar to sulfonic resins (type Amberlite) should be assumed.

In spite of the vast universe of MOFs synthesized to date, the attention of the catalytic community has been focused on a few materials only, due to their unique and outstanding properties for application in catalytic processes [29]. One of these materials is UiO–66, a microporous Zr–MOF with high specific surface area, thermal stability and chemical resistance that is constituted by $Zr_6O_4(OH)_4$ clusters linked by benzenedicarboxylate ligands (BDC) forming a 3D terephthalate structure [30]. It presents an imperfect framework with missing linkers which has given rise to the growing branch of "defect engineering" in MOFs [31–33], because such defects may be useful for establishing interactions with different molecules. So, the vacant sites on nodes in MOFs with missing linkers have been associated with some Lewis acid sites which can bond to reactants and lead to catalysis [34]. Therefore, taking into account the chemical similitude of the zirconium node of the MOFs with zirconia materials and

the high thermal stability of UiO–66, we propose to functionalize the Zr–MOF directly in the inorganic component of this material using the same method adopted to prepare sulfated zirconia [35]. In order to accomplish this purpose, we synthesized UiO–66 nanocrystals with missing linkers and used them as a platform for their post–synthetic acidification through a direct sulfation with ammonium sulfate. In this work, we demonstrate that there is an effective anchoring of SO_x groups in high interaction with the MOF structure that causes the generation of strong acidic surface sites, transforming the S–UiO–66 derivative into a high activity catalyst for a reaction that demands strong acid properties, such as the dimerization of isobutene.

2. Experimental

UiO–66 was prepared by solvothermal synthesis (S1) using a DMF–free protocol reported elsewhere [36] with which a Zr–MOF of high crystallinity and missing linkers was obtained. Subsequently, an S–UiO–66 sample was prepared through incipient wet impregnation with an aqueous solution of ammonium sulfate followed by thermal treatments in He (S1). S–UiO–66 was tested in the gas phase isobutene dimerization using a fixed–bed tubular reactor connected to a continuous flow system and the catalytic measurements were performed at the reaction temperature of 180 °C using a gas mixture of isobutene:He in a 1:4 molar proportion (S2). The materials were characterized by Thermogravimetric analyses (TGA) followed by mass spectrometry, NH_3 temperature–programmed desorption (NH_3–TPD), X–ray diffraction (XRD), Scanning electron microscopy and Energy–dispersive X–ray spectroscopy (SEM–EDS), N_2 adsorption–desorption isotherms, UV–VIS Diffuse reflectance spectroscopy (DRS), Infrared spectroscopy (FTIR) and X–ray photoelectron spectroscopy (XPS). A detailed

description of the synthesis procedures, conditions of material characterization methods and catalytic measurements are provided in the supporting information file.

3. Results and Discussion

3.1. Stabilization of sulfate-type species and development of acidity

The TGA of UiO–66 (Figure 1a) showed a first mass loss due to weakly physisorbed water (50–125 °C) leaving the MOF with all its free porosity [36]; then, a dehydroxylation of the zirconium cluster (125–300 °C) and finally, above 400 °C, the collapse of the structure, indicating a high thermal stability of this prepared UiO–66 material which was similar to that reported when synthesized under other conditions [31–33]. These processes were also simultaneously verified by mass spectrometry of the evolved gases (Figure 1b). From the TGA it was determined, according to reported procedures [31, 33], that this structure had about 3 missing linkers providing a $Zr_6O_{4.6}(OH)_{8.8}$ cluster (S2). On the other hand, the impregnated MOF (S–UiO–66), in addition to the loss of physisorbed water and dehydroxylation, showed a concomitant decomposition of ammonium sulfate (Figure 1c) giving ammonia and water evolutions (Figure 1d) as revealed from mass spectrometry peaks (see also Table S1). The interaction of ammonium sulfate with the structure of the MOF was evident since the stages of decomposition of the free salt occurred at higher temperatures (Figure S1). Subsequently, there was a loss of water, ammonium and sulfur oxides (in the range of 225–360 °C) corresponding to processes of partial precursor decomposition. Finally, the stabilization of a large amount of SO_x species in the UiO–66 structure was also verified when a release of SO_x species was detected in the mass spectrometer at the same time as the MOF collapsed around 560 °C (Figure 1d).

Through the study by thermal desorption of ammonia (NH_3–TPD) it was corroborated that UiO–66 crystals treated in He at 230 °C (UiO–66–230) exhibited acidity distributed in two types of sites of weak and medium strength (Figure 2). The sulfated MOF treated at the same temperature (S–UiO–66–230) also showed an equivalent acidity (Figure 2). In addition UiO–66 pre–treated with He at 350 °C (UiO–66–350) maintained a similar type and amount of acidity with a small amount of strong sites. The amount of these acid sites of different strength in each solid was determined by the quantity of ammonia desorbed per gram of sample in their respective NH_3–TPD test (Figure S2). It should be remarked that, when this same thermal treatment was applied to the sulfated UiO–66 sample (S–UiO–66–350) a large number of strong acid sites developed (Figure 2), related to the SO_x groups anchored and interacting with the MOF. In short, the distribution of surface acidity in these sulfated UiO–66 materials can be tailored by the pre–treatment conditions giving place to a material with strong acid centers able to be used as heterogeneous catalyst at relatively high temperatures (up to 350 ºC).

The synthesized UiO–66 corresponds to a pure and highly crystalline phase, showing the main XRD signals of the (111), (200) and (600) planes of this structure (Figure 3A), and this diffractogram also matches with that simulated from their crystallographic data (CCDC 733458). As it can be observed, all sulfated samples including S–UiO–66–350 (red curve) are highly crystalline solids in which the structure of the MOF is largely preserved. The peaks are slender, analogous to those observed for this MOF synthesized under other conditions of synthesis with a similar crystal size [30]. Moreover, the thermal degradation of UiO–66 could develop phases of tetragonal zirconia whose main signals were located at 29.9°, 35.0°, 50.1° and 59.8° as shown in Figure S3 for a thermally degraded UiO–66 sample. In this regard, as shown in Figure

3A, there was no incipient crystalline phase of segregated zirconia in the sulfated–modified MOF. Additionally, for the sample subjected to catalytic reaction for 18 h, some small extra signals (marked with an asterisk) developed, which could be from crystallized carbonaceous deposits. The diffractograms of the sulfated samples show that the strong acidity developed in S–UiO–66–350 is intrinsic to the modified structure of the MOF, caused by a strong interaction between anchored SO_x groups and the framework upon the high temperature thermal treatment.

UiO–66 crystals corresponded to small nanoparticles (~ 150 nm) forming aggregates in the shape of clusters and this morphology was altered neither in the impregnated UiO–66 nor in the S–UiO–66–230 and S–UiO–66–350 samples (see Figure S4 where scanning electron microscopy images are displayed). In the latter, the average bulk Zr/S ratio was 1.43 which was only slightly higher than that of the impregnated UiO–66 and S–UiO–66–230 samples (Figure S4 also displays the EDX analysis of the samples) showing that a high amount of sulfur was retained in the S–UiO–66–350 sample. The fresh MOF presented a BET surface area of 855 m^2/g while for the S–MOF–350 sample was of 408 m^2/g, which can be explained by the large number of sulfate species introduced in the MOF that reduced the free porosity. Moreover, the contribution of some distortion of the MOF network was also possible although, as it can be noticed, the S–MOF material retained its crystal structure (XRD) and the isotherms remained to be of Type I (Figure S5).

3.2. Interaction of SO_x species with the structure of the MOF

From the UV–VIS spectra obtained for unmodified MOF an intense signal at 245 nm can be observed with a broad shoulder at 285–320 nm and a band-edge at 314 nm (Figure 3B) which is in agreement with previously reported data for this MOF [37, 38]. These bands were attributed to π–π^* electronic transitions of the aromatic ring that can

shift with the presence of substituent functional groups modifying the energy involved in such transitions. These UV–VIS signals are also sensitive to ligand–metal charge transfer (LMCT) processes within the structure of metal–organic frameworks [39, 40]. From the spectra shown in Figure 3B it is evident that for all sulfated UiO–66 samples no significant changes in the spectral profiles can be observed. If very small ZrO_2 crystallites (<1 nm) were present they should produce intense signals around 210–230 nm, which are typical of the octa–coordinated zirconium in the oxide due to O^{2-}–Zr^{4+} charge transfer transitions and a broad peak at 280–300 nm due to defects such as oxygen vacancies [41, 42]. An UV–VIS DRS analysis of a sulfated zirconia sample (Figure S6a) clearly shows how this solid has intense signals below 228 nm, added to a quite strong and broad signal extended from 250 up to 400 nm. This is in line with what was discussed above about the spectra of Figure 3B, where these characteristics were not observed at the same time as the spectral profile of UiO–66 structure was preserved. In short, the UV–VIS spectra are in line with XRD results and demonstrate that the MOF matrix is preserved after the ammonium sulfate incorporation and after its thermal treatments, so the anchored SO_x groups do not modify the ligand also ruling out the segregation of small ZrO_2 domains.

The infrared spectrum of UiO–66 exhibits the characteristic signals of this MOF (Figure 4a), the doublet at 1578 cm^{-1} and 1400 cm^{-1} being the most intense due to the stretching in and out of the plane of the carboxylate groups, respectively, in the terephthalate structure [30]. A signal at 1705 cm^{-1} can also be noticed which could be of C=O stretching of some un–connected COO^- groups in defective regions of this MOF [43, 44]. At lower frequencies (750–400 cm^{-1}) several OH and CH bending modes are mixed with those of Zr–O vibrations of the MOF cluster. Some of these were identified such as the μ_3–O stretching (669 cm^{-1}), μ_3–OH in–phase stretching (480 cm^{-1}) and μ_3–OH

antiphase stretching (454 cm^{-1}) from the oxide and hydroxide bridges, respectively, and also the Zr–(OC) asymmetric stretching mode (555 cm^{-1}) [38, 45]. S–UiO–66–350 maintains the spectral profile (Figure 4f) without showing widening in the carboxylate region, which characterizes an ordered bond connection environment of the 3D structure of this MOF [36]. In addition, all sulfated samples show strongly overlapping absorptions in the 1300–600 cm^{-1} region coming from multiple ν S=O and ν S–O bond vibrations of surface sulfate species [46]. Some of these bands can be associated with bridging bidentate sulfate species, such as those at 1240, 1170–1105, 1048, 996, 961 and 617 cm^{-1} [46, 47]. The signals in the S–UiO–66 very close resemble those from ν S=O and ν S–O vibrations in bridging bidentate sulfate coordinated to zirconium cations in sulfated zirconia [46, 48], that was also verified for a sulfated zirconia material (Figure S6b). In addition, a contribution of a shoulder at 1231 cm^{-1} could be of hydrosulfate species [47] (see also Table S2). Moreover it has been pointed out that in solids with high sulfur loading, as in our case, the broad absorption over 1000–1300 cm^{-1} could be also from other species such as pyrosulfate and multilayer sulfate species [46]. On the other hand, S–UiO–66–350 shows an increased intensity and red shift (12 cm^{-1}) of the 1700 cm^{-1} C=O band, evidencing an interaction of SO_x groups with this environment of the MOF. Furthermore, a noticeable red shift of 9 cm^{-1} and 7 cm^{-1} of the μ_3–O and Zr–(OC) bands, respectively, can also be observed in this sample (Figure 4f, Table S2), reflecting a weakening of these bonds by an electronic interaction with the anchored SO_x groups. The bands of other sites with potential reactivity of the hexacirconium cluster [49, 50] were not modified in the S–UiO–66 samples (Table S2).

The impregnated UiO–66 material exhibits a characteristic Zr 3d XPS spectrum (Figure 5a) compatible with Zr^{4+} in the structure of the MOF [51, 52], which splits into a Zr $3d_{5/2}$ line at 183.2 eV (FWHM = 1.8) and the corresponding Zr $3d_{3/2}$ at 185.6 eV

(FWHM = 1.7). The characteristics of these zirconium species (BE and FWHM) are similar in the S–UiO–66–230 sample (Figure 5b). On the contrary, there are some clear differences in the S–UiO–66–350 solid. Firstly, the XPS signals widen in about 0.2–0.3 eV (Zr $3d_{5/2}$ at 183.5 eV (1.9) and Zr $3d_{3/2}$ at 185.9 eV (2.1)), giving an account of the appearance of zirconium species with a new environment. Secondly, the Zr 3d spectrum of S–UiO–66–350 can be correctly adjusted considering that Zr $3d_{5/2}$ and Zr $3d_{3/2}$ peaks present another zirconium species at about 184.0 eV (1.7) and 186.4 eV (1.8), respectively (Figure 5c). The increase in the BE of these new components could be attributed to a decreased electron density around some zirconium atoms because of their strong interaction with sulfate species. This chemical shift is similar to that generated by the effect of electron extraction of sulfate groups in sulfated zirconia solids that increase the Lewis acidity of the Zr^{4+} species [46, 53]. Moreover, the S 2p region in the sulfated MOF samples exhibits a single symmetric signal at a BE around 169.4 eV (Figure S7a) which is in agreement with the energy of superficial sulfate–type species [53]. In addition, a signal of O 1s can be observed at a BE around 532.0 eV (Figure S7b) which is higher than that from the lattice oxygen corresponding to Zr–O bonds in the MOF (~530 eV) [52] and is also in line with the high BE of the oxygen in sulfate groups [53]. On the other hand, the atomic Zr/S surface ratios for S–UiO–66–230 and S–UiO–66–350 samples were 1.2 and 1.4, respectively, agreeing quite well with their bulk relationships obtained from EDX analysis (Figure S4).

Taking into account the evidence by FTIR and XPS that shows the disposition of anchored SO_x groups in a large proportion as bridging sulfate species coordinated to zirconium atoms of the MOF node, added to the Zr/S ratio close to 1.5 found by both EDS and XPS, we can propose a possible distribution pattern of SO_x species in the MOF. The picture is that in the fully dehydroxylated hexa–zirconium cluster of the S–

UiO66–350 sample, an average of four sulfate groups are connected through O–S–O bridges to adjacent zirconia atoms of the same inorganic node of the MOF, strongly interacting with this cluster. This arrangement of sulfate species would resemble that found in sulfated zirconia solids.

3.3. Catalytic performance in the gas phase dimerization of isobutene

UiO–66–230, UiO–66–350, and S–UiO–66–230 samples presented a very low activity in the gas phase dimerization of isobutene (X isobutene < 1%). Because of the moderate acidity of these materials (Figure 2) their strength was not sufficient to activate this reaction, so only traces of 2,4,4 trimethyl–1 pentene (1P) and 2,4,4 trimethyl–2–pentene (2P) products were observed. In contrast, the S–UiO–66–350 sample showed a remarkable boosting of the catalytic activity (Figure 6a) that reflected the effective strong acidity of this material, which allowed the activation of this demanding reaction. By prolonging the assay for 6h, a progressive deactivation was noted, probably due to light polymeric by–products adsorbed on the active sites. The catalytic results presented in Figure 6a prove the high acidity of the S–UiO–66–350 solid and also show that its performance is better than that of a commercial sulfated zirconia, which probably shows acid centers similar in nature to the S–UiO–66–350 sample, when evaluated under identical conditions. It can be noticed how S–UiO66–350 had a higher intrinsic activity, and at the same time that the decrease of activity with time on stream was lower (Figure 6b) which was verified in a repeated test, proving the catalyst performance reliability. This behavior reveals some differences in the physical–chemical characteristic of the active sites exposed in S–UiO66–350 with respect to those in sulfated zirconia. Therefore, it should also be mentioned that the selectivity (or products distribution) obtained with S–UiO–66–350 was not the same as when using sulfated zirconia as catalyst (Figure S8). As a tentative explanation, the confinement effect

induced by the MOF structure over the strong acid sites of the S–UiO–66–350 catalyst could be the reason for these selectivity modifications. In order to check the reversibility of the loss of activity with the time in reaction, the S–UiO–66–350 catalytic sample after 6h in reaction, was treated in He flow at the initial pretreatment temperature of 350 °C for 1h (Figure 6c). With this thermal heating the catalyst was highly reactivated, practically recovering its initial performance. The dimerization reaction generally causes a gradual deactivation of catalyts by deposition of carbonaceous species, due to the acidic nature of the active sites. The fact that with a heat treatment in He the activity of S–UiO–66–350 was recovered, strongly suggests that it is due to a cleaning of such sites which regenerate their activity. Since the recovery was almost total, it can be thought that these deposits are of light carbonaceous species. The repetition of successive evaluation–reactivation cycles shows, on the one hand, that the deactivation phenomenon was largely reversible and on the other hand, the high long–term stability of S–UiO–66 under reaction. Moreover, the catalyst subjected to the successive reaction tests as well as to reaction–reactivation cycles retained the structural features (XRD patterns and DRS UV spectra) of the original UiO–66 as shown in Figure 3.

It is shown that S–UiO–66 required a relatively high temperature treatment (350 °C) to generate an active solid with strong acidity (Figure 2), remaining stable at this temperature (Figure 3). Thus, this pretreatment carried out in–situ prior to the catalytic test, ensured on the one hand that the activated S–UiO–66–350 was completely dehydrated (Figure 1) and on the other hand that the sulfate groups anchored on the structure of the MOF, reacted to develop a strong interaction with the Zr–hexacluster of the inorganic nodes causing an electron withdrawal effect (Figures 4 and 5) and boosting the Lewis acidity. This type of surface acid centers seems to be similar to that of $S–O_x$ groups anchored on zirconia after conventional sulfation processes [35] i.e. the

catalytic species formed on the Zr_6O_9 nodes of MOF mimic the sites on sulfated zirconia. This is also consistent with the fact that a treatment of S–UiO–66 at a lower temperature (230 °C) does not generate such acid centers. In brief, the grouping of Zr–O atoms of the inorganic brick of the MOF modified by sulfates provides a type of acidity similar to that found in sulfated zirconia, which is stable under high temperature reaction conditions. This is in contrast with solids having Bronsted–type acidity, which exhibit an acid functioning mechanism that requires the presence of water molecules on the surface of the material to provide proton transfer, such as in the case of reported sulfated MOF–808 [28]. For this reason, the solids prepared in this latter case are not stable at moderate temperatures, and after losing surface water molecules, such as in sulfonic resins, they become irreversibly deactivated [28]. In the case of the S–UiO–66–350 material, it provides an acid mechanism similar to that of sulfated zirconia to promote isobutene dimerization. Hence, the nature of such acid centers can be related to Lewis acidity [35] which predominates in the absence of water vapor and after calcination at high temperature. These acid sites are also probably tuned by the three–dimensional porous environment and by the organic nature of the ligands that surround these sites, which is reflected in the lower deactivation rate in comparison with conventional sulfated zirconia (Figure 6 a), and in the shift of the products distribution (Figure S8). Notice that under our reaction conditions the presence of both water and hydrogen was ruled out, so that a transformation of the Lewis acids sites into Brönsted sites was discarded.

4. Conclusions

To sum up, it is demonstrated an effective anchoring of SO_x groups in the UiO–66 Zr–Metal–Organic Framework through a simple and green (without using harsh

reactants) direct post-synthetic sulfation procedure, giving rise to the S-UiO-66-350 derivative which preserves the structural qualities of the original MOF. The sulfate-type species interact with the MOF close to their inorganic node environments, generating a strong acidity which allows activating a gas phase reaction with demand of strong acid sites, such as the dimerization of isobutene. In addition, the S-UiO-66-350 solid can be reactivated with short treatments in He, recovering much of the initial activity and allowing its use for 18 h at 180 °C without altering its physical-chemical characteristics. The robust behavior of S-UiO-66-350 in this reaction makes us anticipate its general applicability to other heterogeneous catalytic reactions in gas phase with strong acid demand.

Acknowledgments

We acknowledge the financial support from the Spanish Government (projects CTQ2017-89443-C3-1-R and CTQ2017-89443-C3-3-R). Juan M. Zamaro thanks CONICET of Argentina for the support given to carry out a research stay at ICP-CSIC, Spain.

Appendix A. Supplementary material

A detailed description of the synthesis procedures, material characterization methods and catalytic measurements is provided.

References

1. Yuanjing Cui, Bin Li, Huajun He, Wei Zhou, Banglin Chen, Guodong Qian, Metal-Organic Frameworks as Platforms for Functional Materials, Acc. Chem. Res. 49 (2016) 483-493.

2. Jarad A. Mason, Mike Veenstra, Jeffrey R. Long, Evaluating metal–organic frameworks for natural gas storage, Chem. Sci. 5 (2014) 32–51.

3. Chunbai He, Demin Liu, Wenbin Lin, Nanomedicine Applications of Hybrid Nanomaterials Built from Metal–Ligand Coordination Bonds: Nanoscale Metal–Organic Frameworks and Nanoscale Coordination Polymers, Chem. Rev. 115 (2015) 11079–11108.

4. Chun–Yi Sun, Chao Qin, Xin–Long Wang, Zhong–Min Su, Metal–organic frameworks as potential drug delivery systems, Expert Opin. Drug Deliv. 10,1 (2013) 89–101.

5. Jie Li, Xiangxue Wang, Guixia Zhao, Changlun Chen, Zhifang Chai, Ahmed Alsaedi, Tasawar Hayat, Xiangke Wang, Metal–organic framework–based materials: superior adsorbents for the capture of toxic and radioactive metal ions, Chem. Soc. Rev. 47 (2018) 2322–2356.

6. Yingmu Zhang, Shuai Yuan, Gregory Day, Xuan Wang, Xinyu Yang, Hong–Cai Zhou, Luminescent sensors based on metal–organic frameworks, Coord. Chem. Rev. 354 (2018) 28–45.

7. Yuan–Biao Huang, Jun Liang, Xu–Sheng Wang, Rong Cao, Multifunctional metal–organic framework catalysts: synergistic catalysis and tandem reactions, Chem. Soc. Rev. 46 (2017) 126–157.

8. Bin Li, Hui–Min Wen, Yuanjing Cui, Wei Zhou, Guodong Qian, Banglin Chen, Emerging Multifunctional Metal–Organic Framework Materials, Adv. Mater. 28 (2016) 8819–8860.

9. Long Jiao, Yang Wang, Hai–Long Jiang, Qiang Xu, Metal–Organic Frameworks as Platforms for Catalytic Applications, Adv. Mater. 30 (2018) 1703663.

10. Panchenko, V.N. Matrosova, M.M., Jeon, J., Jun, J.W., Timofeeva, M.N., Jhung, S.H., Catalytic behavior of metal–organic frameworks in the Knoevenagel condensation reaction, J. Catal. 316 (2014) 251–259.

11. B. Murillo, B. Zornoza, O. de la Iglesia, C. Téllez, J. Coronas, Chemocatalysis of sugars to produce lactic acid derivatives on zeolitic imidazolate frameworks, J. Catal. 334 (2016) 60–67.

12. A. Chatterjee, X. Hu, F. L–Y. Lam, Towards a recyclable MOF catalyst for efficient production of furfural, Catal. Today 314 (2018) 129–136.

13. H–C. Lee, M. Antonietti, B. V. K. J. Schmidt, A Cu(II) metal–organic framework as a recyclable catalyst for ARGET ATRP, Polym. Chem., 7 (2016) 7199–7203.

14. Yogesh C. Sharma, Bhaskar Singh, John Korstad, Advancements in solid acid catalysts for ecofriendly and economically viable synthesis of biodiesel, Biofuels, Bioprod. Bioref. 5 (2011) 69–92.

15. Nele Reimer, Bart Bueken, Sebastian Leubner, Christopher Seidler, Michael Wark, Dirk De Vos, Norbert Stock, Three Series of Sulfo–Functionalized Mixed–Linker CAU–10 Analogues: Sorption Properties, Proton Conductivity, and Catalytic Activity, Chem. Eur. J. 21 (2015) 12517–12524.

16. Young–Min Chung, Hee–Young Kim, Wha–Seung Ahn, Friedel–Crafts Acylation of p–Xylene over Sulfonated Zirconium Terephthalates, Catal. Lett. 144 (2014) 817–824.

17. Maw Lin Foo, Satoshi Horike, Tomohiro Fukushima Yuh Hijikata, Yoshiki Kubota, Masaki Takata, Susumu Kitagawa, Ligand–based solid solution approach to stabilisation of sulphonic acid groups in porous coordination polymer $Zr_6O_4(OH)_4(BDC)_6$ (UiO–66), Dalton Trans. 41 (2012) 13791–13794.

18. Chufan Kang, Yaguang Peng, Yuanzhe Tang, Hongliang Huang, Chongli Zhong, Sulfate–Rich Metal–Organic Framework for High Efficiency and Selective Removal of Barium from Nuclear Wastewater, Ind. Eng. Chem. Res. 56 (2017) 13866–13873.

19. Jinzhu Chen, Kegui Li, Limin Chen, Ruliang Liu, Xing Huang, Daiqi Ye, Conversion of fructose into 5–hydroxymethylfurfural catalyzed by recyclable sulfonic acid–functionalized metal–organic frameworks, Green Chem. 16 (2014) 2490–2499.

20. Maarten G. Goesten, Jana Juan–Alcañiz, Enrique V. Ramos–Fernandez, K.B. Sai Sankar Gupta, Eli Stavitski, Herman van Bekkum, Jorge Gascon, Freek Kapteijn, Sulfation of metal–organic frameworks: Opportunities for acid catalysis and proton conductivity, J. Catal. 281 (2011) 177–187.

21. Won Ju Phang, Hyuna Jo, Woo Ram Lee, Jeong Hwa Song, Kicheon Yoo, BongSoo Kim, Chang Seop Hong, Superprotonic Conductivity of a UiO–66 Framework Functionalized with Sulfonic Acid Groups by Facile Postsynthetic Oxidation, Angew. Chem. Int. Ed. 54 (2015) 5142–5146.

22. Juncong Jiang, Felipe Gándara, Yue–Biao Zhang, Kyungsu Na, Omar M. Yaghi, Walter G. Klemperer, Superacidity in Sulfated Metal–Organic Framework–808, J. Am. Chem. Soc. 136 (2014) 12844–12847.

23. Linh H. T. Nguyen, The T. Nguyen, Ha L. Nguyen, Tan L. H. Doan, Phuong Hoang Tran, A new superacid hafnium–based metal–organic framework as a highly active heterogeneous catalyst for the synthesis of benzoxazoles under solvent–free conditions, Catal. Sci. Technol. 7 (2017) 4346–4350.

24. Jinzhu Chen, Kegui Li, Limin Chen, Ruliang Liu, Xing Huang, Daiqi Ye, Conversion of fructose into 5–hydroxymethylfurfural catalyzed by recyclable

sulfonic acid–functionalized metal–organic frameworks, Green Chem. 16 (2014) 2490–2499.

25. Baiyan Li, Yiming Zhang, Dingxuan Ma, Lu Li, Guanghua Li, Guodong Li, Zhan Shi, Shouhua Feng, A strategy toward constructing a bifunctionalized MOF catalyst: post–synthetic modification of MOFs on organic ligands and coordinatively unsaturated metal sites, Chem. Commun. 48 (2012) 6151–6153.

26. Esra Yılmaz, Emine Sert, Ferhan Sami Atalay, Synthesis and sulfation of titanium based metal organic framework; MIL–125 and usage as catalyst in esterification reactions, Catal. Commun. 100 (2017) 48–51.

27. Yen H. Vo, Thanh V. Le, Hieu D. Nguyen, Tuong A. To, Hiep Q. Ha, Anh T. Nguyen, Anh N.Q. Phan, Nam T.S. Phan, Synthesis of quinazolinones and benzazoles utilizing recyclable sulfated metal–organic framework–808 catalyst in glycerol as green solvent, J. Ind. Eng. Chem. 64 (2018) 107–115.

28. Christopher A. Trickett, Thomas M. Osborn Popp, Ji Su, Chang Yan, Jonathan Weisberg, Ashfia Huq, Philipp Urban, Juncong Jiang, Markus J. Kalmutzki, Qingni Liu, Jayeon Baek, Martin P. Head–Gordon, Gabor A. Somorjai, Jeffrey A. Reimer, Omar M. Yaghi, Identification of the strong Brønsted acid site in a metal–organic framework solid acid catalyst, Nature Chemistry 170, 11 (2019) 170–176.

29. Dong Yang, Bruce C. Gates, Catalysis by Metal Organic Frameworks: Perspective and Suggestions for Future Research, ACS Catal. 9 (2019) 1779–1798.

30. Cavka J.H., Jakobsen S., Olsbye U., Guillou N., Lamberti C., Bordiga S., Lillerud K.P., A new zirconium inorganic building brick forming metal organic frameworks with exceptional stability, J. Am. Chem. Soc. 130 (2008) 13850–13851.

31. Greig C. Shearer, Sachin Chavan, Silvia Bordiga, Stian Svelle, Unni Olsbye, Karl Petter Lillerud, Defect Engineering: Tuning the Porosity and Composition of

the Metal–Organic Framework UiO–66 via Modulated Synthesis, Chem. Mater. 28 (2016) 3749–3761.

32. Wu H., Chua Y.S., Krungleviciute V., Tyagi M., Chen P., Yildirim T., Zhou W., Unusual and highly tunable missing– linker defects in zirconium metal–organic framework UiO–66 and their important effects on gas adsorption, J. Am. Chem. Soc. 135 (2013) 10525–10532.

33. Weibin Liang, Campbell J. Coghlan, Florence Ragon, Marta Rubio–Martinez, **Deanna M. D'Alessandro, Ravichandar Babarao, Defect engineering of UiO**–66 for CO_2 and H_2O uptake –a combined experimental and simulation study, Dalton Trans. 45 (2016) 4496–4500.

34. Vermoortele, F.; Bueken, B.; Le Bars, G.; Van de Voorde, B.; Vandichel, M.; Houthoofd, K.; Vimont, A.; Daturi, M.; Waroquier, M.; Van Speybroeck, V.; Kirschhock, C.; De Vos, D. E. Synthesis Modulation as a Tool To Increase the Catalytic Activity of Metal–Organic Frameworks: The Unique Case of UiO–66(Zr). J. Am. Chem. Soc. 135 (2013) 11465–11468.

35. E. Iglesia, S. L. Soled, G. M. Kramer, Isomerization of alkanes on sulfated zirconia: promotion by Pt and by adamantly hydride transfer species, J. Catal. 144 (1993) 238–253.

36. L. A. Lozano, C. M. Iglesias, B.M.C. Faroldi, M. A. Ulla, J.M. Zamaro, Efficient solvothermal synthesis of highly porous UiO–66 nanocrystals in dimethylformamide–free media, J. Mater. Sci. 53 (2018) 1862–1873.

37. Jiao He, Jiaqiang Wang, Yongjuan Chen, Jinping Zhang, Deliang Duan, Yao Wang, Zhiying Yan, A dye–sensitized Pt@UiO–66(Zr) metal–organic framework for visible–light photocatalytic hydrogen production, Chem. Commun. 50 (2014) 7063–7066.

38. Valenzano L., Civalleri B., Chavan S., Bordiga S., Nilsen M.H., Jakobsen S., Lillerud K.P., Lamberti C., Disclosing the complex structure of UiO–66 metal organic framework: a synergic combination of experiment and theory, Chem. Mater. 23 (2011) 1700–1718.

39. Lijuan Shen, Ruowen Liang, Mingbu Luo, Fenfen Jing, Ling Wu, Electronic effects of ligand substitution on metal–organic framework photocatalysts: the case study of UiO–66, Phys. Chem. Chem. Phys. 17 (2015) 117–121.

40. Davood Azarifar, Ramin Ghorbani–Vaghei, Saba Daliran, Ali Reza Oveisi, A Multifunctional Zirconium–Based Metal–Organic Framework for the One–Pot Tandem Photooxidative Passerini Three–Component Reaction of Alcohols, ChemCatChem 9 (2017) 1992–2000.

41. H. Kobayashi, S. Ito, K. Hara, A. Fukuoka, Conversion of glycerol to acrolein by mesoporous sulfated zirconia–silica catalyst, Chin. J. Catal. 38 (2017) 420–425.

42. S. Chakharia, M. Kadri Younes, A. Rives, A. Ghorbel, Effect of the doping agent nature on the characteristic and catalytic properties of aerogel zirconia catalysts doped with sulfate groups or heteropolytungstic acid, Mater. Res. Bull. 72 (2015) 35–42.

43. Jared B. DeCoste, Tyler J. Demasky, Michael J. Katz, Omar K. Farha, Joseph T. Hupp, A UiO–66 analogue with uncoordinated carboxylic acids for the broad–spectrum removal of toxic chemicals, New J. Chem. 39 (2015) 2396–2399.

44. Yi Luan, Yue Qi, Zhaokui Jin, Xiong Peng, Hongyi Gao, Ge Wang, Synthesis of a flower–like Zr–based metal–organic framework and study of its catalytic performance in the Mannich reaction, RSC Adv. 5 (2015) 19273–19278.

45. Chavan S., Vitillo J.G., Gianolio D., Zavorotynska O., Civalleri B., Jakobsen S., Nilsen M.H., Valenzano L., Lamberti C., Lillerud K.P., Bordiga S., H2 storage in

isostructural UiO–67 and UiO–66 MOF, Phys. Chem. Chem. Phys. 14 (2012) 1614–1626.

46. Abdallah I. M. Rabee, Gamal A. H. Mekhemer, Amin Osatiashtiani, Mark A. Isaacs, Adam F. Lee, Karen Wilson, Mohamed I. Zaki, Acidity–Reactivity Relationships in Catalytic Esterification over Ammonium Sulfate–Derived Sulfated Zirconia, Catalysts 7 (2017) 204–219.

47. E. A. Vlasov, S. V. MMyakin, M.M. Sychov, A. Aho, A.Y. Postnov, N.V. Maltseva, A. O. Dolgashev, S.O. Omarov, D.Y. Murzin, On synthesis and characterization of sulfated alumina–zirconia catalysts for isobutene alkylation, Catal. Lett. 145, 9 (2015) 1651–1659.

48. Mishra, M.K.; Tyagi, B.; Jasra, R.V. Synthesis and characterization of nano–crystalline sulfated zirconia by sol–gel method, J. Mol. Catal. A–Chem. 223 (2004) 61–65.

49. H. Giang T. Nguyen, N. M. Schweitzer, C. Chang, T. L. Drake, M. C. So, P. C. Stair, O. K. Farha, J. T. Hupp, S. T. Nguyen, Vanadium–Node–Functionalized UiO–66: A Thermally Stable MOF Supported Catalyst for the Gas–Phase Oxidative Dehydrogenation of Cyclohexene, ACS Catal. 4 (2014) 2496–2500.

50. C. Larabi, E. A. Quadrelli, Titration of Zr_3(μ–OH) Hydroxy Groups at the Cornerstones of Bulk MOF UiO–67, [$Zr_6O_4(OH)_4$(biphenyldicarboxylate)$_6$], and Their Reaction with [AuMe(PMe_3)], Eur. J. Inorg. Chem. 2012 (2012) 3014–3022.

51. Rongbin Zhang, Biao Du, Qiuchan Li, Zuqiang Cao, Gang Feng, Xuewen Wang, α–Fe_2O_3 nanoclusters confined into UiO–66 for efficient visible–light photodegradation performance, Appl. Surf. Sci. 466 (2019) 956–963.

52. Songjian Zhao, Dongyao chen, Haomiao Xu, Jian mei, Zan Qu, Ping Liu, Yong Cui, Naiqiang Yan, Combined effects of Ag and UiO–66 for removal of elemental mercury from flue gas, Chemosphere 197 (2018) 65–72.

53. Muriel A. Ecormier, Karen Wilson, Adam F. Lee, Structure–reactivity correlations in sulphated–zirconia catalysts for the isomerisation of α–pinene, J. Catal. 215 (2003) 57–65.

Figure Legends

Figure 1. TGA–dTGA (He) and the respective monitoring of evolved gases by mass spectrometry for: a, b) UiO–66; c, d) sulfated UiO–66 (The inset in Figure 1d show a small evolution of SO_x at 225–360 °C).

Figure 2. Proportion and strength of acid sites in: a) UiO–66 treated in He at 230 °C (UiO–66–230); b) Sulfated UiO–66 treated in He at 230 °C (S–UiO–66–230); c) UiO–66 treated in He at 350 °C (UiO–66–350); d) Sulfated UiO–66 treated in He at 350 °C (S–UiO–66–350). The a.u. units refer to the total area (per gram of sample) of NH_3–TPD signals integrated at different temperature ranges (50–150 °C weak acid sites, 150–230 °C medium acid sites, 230–350 °C strong acid sites).

Figure 3. XRD patterns (A) and DRS UV spectra (B) of: a) UiO–66; b) UiO–66–230; c) UiO–66–350; d) impregnated UiO–66; e) S–UiO–66–230; f) S–UiO–66–350; g) S–UiO–66–350 after 18 h of catalytic use (the diffractograms were normalized in each case with respect to the peak of maximum intensity, corresponding to 2θ 7.2 °).

Figure 4. FTIR spectra: a) synthesized UiO–66; b) UiO–66–230; c) UiO–66–350; d) impregnated UiO–66; e) S–UiO–66–230; f) S–UiO–66–350.

Figure 5. XPS in the Zr 3d region: a) impregnated UiO–66; b) S–UiO–66–230; c) S–UiO–66–350.

Figure 6. Catalytic behavior of the UiO–66–based catalyst in the gas phase isobutene dimerization: a) Catalytic activity at 180 °C for: S–UiO–66–350 (red circles) and sulfated zirconia (black square), taken over a 6–hour test; b) Comparison of initial conversion values (cyan bar) and percentage of deactivation after 6h of reaction (magenta bar); c) Consecutive evaluation cycles of S–UiO–66–350 extended for a total period of 18h with regeneration steps interspersed at 6 h and 12 h by treatments with He at 350 °C for 60 min.

Supporting Information

Direct sulfation of a Zr-based Metal-Organic Framework to attain strong acid catalysts

José M. Fernández-Morales[1], Luis A. Lozano[2], Eva Castillejos-López[1], I. Rodríguez-Ramos[3], A. Guerrero-Ruiz [1], Juan M. Zamaro[2,3]

[1] Dpto. Química Inorgánica y Técnica, Facultad de Ciencias UNED, Senda del Rey 9, 28040 Madrid, Spain

[2] Instituto de Investigaciones en Catálisis y Petroquímica, INCAPE (FIQ, UNL, CONICET). Santiago del Estero 2829 (3000), Santa Fe, Argentina

[3] Instituto de Catálisis y Petroleoquímica, CSIC, Marie Curie 2, 28049 Madrid, Spain

KEYWORDS

Zirconium-MOF, UiO-66, sulfate functions, acidity, isobutene dimerization.

Table of contents

S1. Synthesis procedures

a) Synthesis of UiO-66 crystals

Benzenedicarboxylic acid (BDC, Aldrich), $ZrCl_4$ (Aldrich) and acetone (Cicarelli, 99.0% purity) were used without further purification. The mixture procedure basically consisted in mixing the two solid reactants together with the solvent in the molar proportions BDC:$ZrCl_4$:solvent = 1:1:1622. After obtaining the homogeneous mixture, it was placed under solvothermal treatments at 80 °C for 24h. At the end of the treatments, the solids were recovered by centrifugation (10000 rpm, 10 min), washed twice with ethanol and finally dried at 80 °C overnight.

b) Obtention of S-UiO-66 by post-synthetic sulfation

First, the volume of water absorption of the synthesized UiO–66 crystals was determined and then 200 mg of the MOF was impregnated to incipient humidity using an aqueous solution containing 64 mg of ammonium sulfate (Sigma–**Aldrich, ACS reagent, purity ≥ 99%). The** impregnated sample was allowed to dry at room temperature in a hood overnight and then in an oven at 90 °C, overnight. The dry solid was homogenized in agate mortar to disaggregate the sample, leaving a fine homogeneous powder. The sample thus prepared was placed in a quartz reactor and heated in He (20 cm^3 min^{-1}) at 5 °C min^{-1} brought to 350 °C for 60 min and finally cooled in He up to 180 °C being ready for its catalytic test.

S2. Characterizations and catalytic tests

a) Catalytic evaluation in gas phase isobutene dimerization

The catalytic activity of the samples was evaluated in a fixed–bed tubular reactor connected to a continuous flow system PID Eng&Tech, which was heated by a furnace with a PID control and equipped with mass flow controllers (Bronkhorst High–Tech B.V. mod. EL–Flow Select). Prior to the catalytic tests, the sample of sulfated MOF (50 mg) was activated as described above. After that, the system was cooled and the catalytic runs were performed using a gas mixture of isobutene:He in a 1:4 molar proportion employing a total gas flow of 8 cm^3 min^{-1}. The catalytic measurements were performed after carrying the sample in He at the reaction temperature (180 °C), after which the gas stream was changed to admit the reagent. After maintaining 5 min in reaction atmosphere to stabilize, conversion measurements were taken every 10 min. The isobutene conversions were determined by analyzing the exit gas with an on–line Varian CP–3800 chromatograph with a FID detector (200 °C, detection range 10) and a Supelco alumina sulfate **PLOT capillary column (30m x 0'53mm/10um). First, it was kept at** 120 °C for 5 min; then a ramp of 15 °C min^{-1} was applied up to 180 °C and maintained at this temperature for 10 min. Isobutane conversions were calculated as: $X_{Ib} = ([Ib]° - [Ib])/[Ib]° \times 100$; where X_{Ib} is % conversion, [Ib]° and [Ib] are inlet and outlet gas concentrations, respectively. Catalytic tests were carried out in duplicate, verifying that the solids exhibited a repetitive behavior.

b) Thermogravimetric analyses with mass spectrometry

To analyze the thermal evolution of UiO–66 and sulfated UiO–66 samples thermogravimetric analyses (TGA) were conducted with an equipment TA Instruments

SDT Q600 TA from 30 °C to 900 °C at 10 °C min^{-1} in He flow (50 cm^3 min^{-1}, STP). The output gases from TGA were monitored by mass spectrometry using a ThermoStar GSD 301 T3 instrument (filament 150 °C, SEM and emission detector at 950 mV).

c) X-ray diffraction

Samples were analyzed by X-ray diffraction (XRD) using a Polycrystal X'Pert Pro PANalytical diffractometer with Ni-filtered Cu/K radiation (λ= 1.54 Å) operating at 45 kV and 40 ° mA. For each sample, Bragg's angles between 4° and 90° (soller slit opening 0.04 rad, sample spinning 2s, step size 0.04° and counting time 100 s).

d) UV-VIS Diffuse reflectance spectroscopy (DRS)

UV measurements were performed with a Varian Cary 5000 UV/VIS spectrometer with a 110 mm diameter diffuse reflectance sphere accessory. The equipment is of double beam, equipped with a photomultiplier type detector (PMT), double shutter electronically synchronized and double dispersive system with holographic diffraction gratings. The tests were carried out between 200–900 nm with a scanning speed of 200 nm min^{-1}.

e) Acidity by ammonia temperature-programmed desorption

The acidity was determined by static ammonia adsorption using an ASAP 2010 Micromeritics unit with a working range from 0 to 950 mmHg. The adsorption was carried out at 50 °C and 50 mg of material were analyzed. For both the synthesized MOF and the sulfated MOF, the sample was first pretreated in He at 230 °C (5 °C min^{-1}) for 60 min after which it was cooled to 50 °C and NH_3 was adsorbed for 30 min. After sweeping with He the TPD was carried out at 10 °C min^{-1}, finishing at 230 °C and maintaining at this temperature for 30 min. It was then cooled in He and another pretreatment in He was carried out (5 °C min^{-1}) up to 350 °C and maintained for 60 min. Then, the same TPD test described above was carried out, with a maximum temperature of 350 °C.

f) Scanning electron microscopy and Energy-dispersive X-ray spectroscopy

The microstructure of the solids obtained was examined by scanning electron microscopy (SEM) with a benchtop instrument Hitachi model TM–1000 with a backscattered electrons detector operated at 15 kV. Elemental microanalyses were carried out by energy–dispersive X–ray spectroscopy (EDS) coupled to the SEM instrument.

g) Infrared spectroscopy

Fourier transformed infrared spectroscopy (FTIR) of KBr–compacted samples was performed with a Thermo Nicolet Nexus 670 instrument equipped with a DTGS detector (400–4000 cm^{-1}, 60 scans, 2 cm^{-1} resolution).

h) Nitrogen adsorption-desorption isotherms

Adsorption–desorption isotherms of N_2 at 77 K were acquired with a Micromeritics ASAP 2020 unit. Prior the assay the solids were degassed (4 h, 200 °C) and then isotherms up to a p/p° 1 E–06 were obtained and the specific surface area (BET) were also calculated.

i) X-ray photoelectron spectroscopy

Sample surface was examined by X–ray photoelectron spectroscopy (XPS) with a Multitechnique Specs module. The binding energies (BE) of Zr 3d were analyzed. The spectra were obtained with a pass energy of 30 eV with a Mg anode operated at 200 W. The samples were supported on the sample holder, subjected to vacuum dehydration at 100 °C for 15 min and finally evacuated under vacuum, prior to the readings. The peak of C 1s at 284.8 eV was taken as internal reference. The data processing and peak deconvolution were performed using the Casa XPS software, adjusting the peaks by means of a Gaussian:Lorentzian waveform (70:30). after subtracting a base of type Shirley and determining the area by integration. The Zr 3d signals were determined considering 2.4 eV the separation between the Zr $3d_{3/2}$ and Zr $3d_{5/2}$

levels with an intensity ratio of 2:3, respectively. The shift of the BE energies due to surface charges was minimized by operating the instrument in flow gun mode.

S3. Estimation from TGA of the missing linkers and the formal composition of the synthesized defective UiO-66.

	W_0 (g)	$\%RW_1$	$\%RW_2$	$\%RW_3$	$\%RW_4$
UiO-66	0.01136	70.97	66.56	64.50	38.60

W_0 is the initial mass of the TGA and $\%RW_i$ is the relative weight at point i:

$\%RW_1$ at 150 ° C: total evacuation of the host molecules.
$\%RW_2$ at 280 ° C: total dehydroxylation.
$\%RW_3$ at 375 °C: combustion of the linker begins
$\%RW_4$ at 625 °C: structural collapse.

(Each point was taken where the derivative ends, with the exception of point 3 that was taken where it begins)

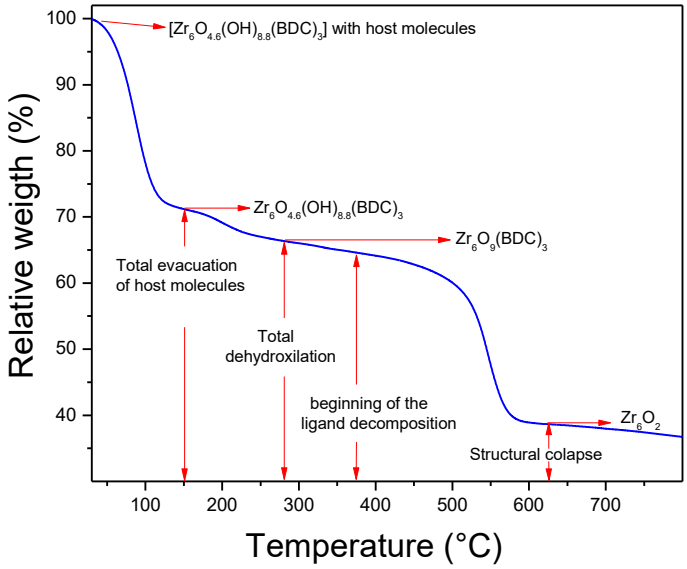

The structural defects in UiO-66 and their respective molecular compensation can be evidenced and quantified by TGA. In these calculations, the following was taken into account:

We rule out losses of zirconium; therefore, the structural defects are related to the linker deficiency and their number is quantified per Zr_6 cluster unit.

A general formula is obtained for a defective UiO-66 sample in which evacuations have already occurred due to desolvation, i.e. the material is considered in an "evacuated" state when only the zirconium oxide connectors and the BDC linkers remain. Therefore, it is assumed that each loss of linker is compensated by an additional oxide anion in the cluster [1], which gives the following average MOF composition in that state:

Where is the number of linker deficiencies per unit Zr_6.
Through XRD it can be seen that the structural collapse results in ZrO_2. The actual amount of ZrO_2 obtained from the starting sample is:

Knowing that corresponds to the BDC loss from the structure, the actual amount of BDC obtained from the starting sample is:

Since it is assumed that there is no Zr loss, for every BDC mole in a perfect UiO-66 structure, 6 mol of ZrO_2 should be obtained by decomposition. The actual amount of BDC that makes up the molecular structure of the MOF is:

According to what was previously assumed, the molecular formula of our evacuated UiO-66 (with the loss of linkers) is:

The amount of our evacuated UiO-66 is:

The actual dehydroxylated mass of the sample is estimated knowing that corresponds to the dehydroxylation of the structure:

The amount of dehydroxylated UiO–66 is:

The molar ratio of dehydroxylated UiO–66 and the dehydroxylated moles is:

Therefore, the dehydroxylation reaction of our UiO–66 is:

Whereas the dehydroxylation of a perfect UiO–66 (without vacancies) is:

Then, the theoretical molar ratio of dehydroxylated UiO–66 and the dehydroxylated moles is equal to 0.5. This value is greater than the experimental ratio because, as demonstrated by some authors [2], the BDC losses in the structure are compensated with hydroxyls.

Molecular formula of defective UiO–66 in its different states

Dehydroxilated UiO-66	Hydroxilated UiO-66
$Zr_6O_9(BDC)_3$	$Zr_6O_{4.5}(OH)_{8.8}(BDC)_3$

1. G. C. Shearer, S. Chavan, S. Bordiga, S. Svelle, U. Olsbye, K. P. Lillerud, Defect Engineering: Tuning the Porosity and Composition of the Metal–Organic Framework UiO–66 via Modulated Synthesis, Chem. Mater. 28 (2016) 3749–3761.
2. W. Liang, C. J. Coghlan, F. Ragon, M. Rubio-**Martinez, D. M. D'Alessandro, R. Babarao, Defect engineering** of UiO–66 for CO_2 and H_2O uptake –a combined experimental and simulation study, Dalton Trans. 45 (2016) 4496–4500.

Table S1. Proportions detected by mass spectrometry of the main and secondary fragments of water and ammonia released during TGA. Comparison with the natural populations of the fragments of indicated evolved molecules are presented.

Ratio of mass fragments	Natural Proportions[1]	$(NH_4)_2SO_4$		UiO-66			Impregnated UiO-66				
		283 [2]	385	71	176	549	66	180	212	300-350	569
m18/m17	(H_2O) 4.7	0.5	0.4	4.1	4.3	4.4	4.5	1.1	1.1	2.3	4.4
m17/m16	(NH_3) 1.2	0.9	1.3	-	-	*	-	1.6	1.6	0.2	*

[1] Taken from "Eight peak Index of Mass Spectra", The Royal Society of Chemistry, 3th edition, 1983.
[2] Temperature of the TGA evolutions

m18 (H_2O): H_2O fragment
m17 (H_2O): OH fragment

m17 (NH_3): NH_3 fragment
m16 (NH_3): NH_2 fragment

* A fragment of m16 due to CH_4 evolution was observed.

Table S2. Positions of the bands on the infrared spectra (cm^{-1}).

Sample	MOF [1]	SO_x
UiO-66 UiO-66-230 UiO-66-350	1705 1578 1508 1400 1018 746 669 555 480 454	
Impregnated UiO-66	1705 1578 1508 1400 1018 746 669 555 480 454	1285 1240 1231 1156 1113 1048 996 961 779 734 617
S-UiO-66-230	1694 [2] 1578 1508 1400 1018 746 669 555 480 454	1285 1240 1231 1156 1113 1048 996 961 779 734 617
S-UiO-66-350	1693 [2] 1578 1508 1400 1018 746 659 [2] 548 [2] 480 454	1285 1240 1231 1156 1113 1048 996 961 779 734 617

[1] The most important bands in the skeletal region of UiO-66.
[2] The signals that shift the vibration frequency are indicated in red letters.

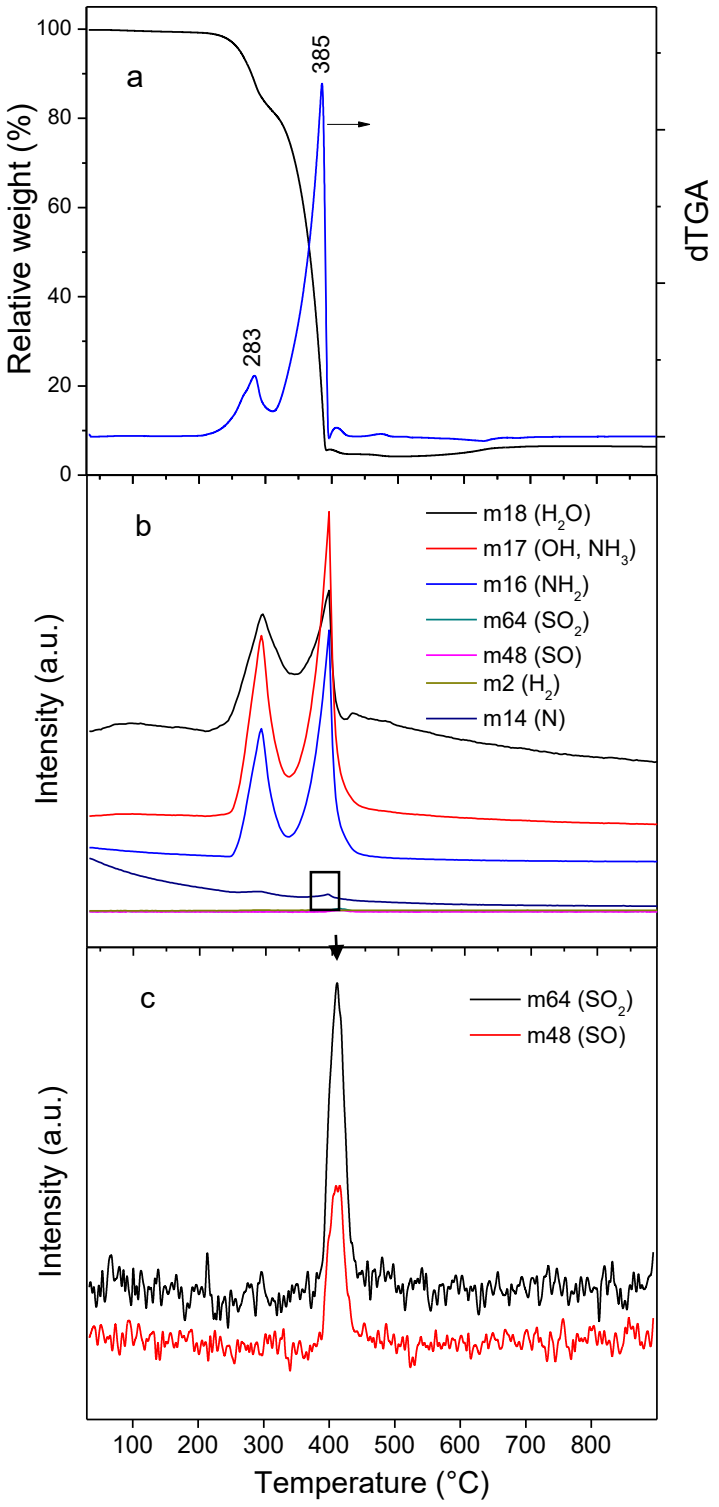

Figure S1. TGA-dTGA (He) profiles of $(NH_4)_2SO_4$ salt and the corresponding evolved gases followed by mass spectrometry.

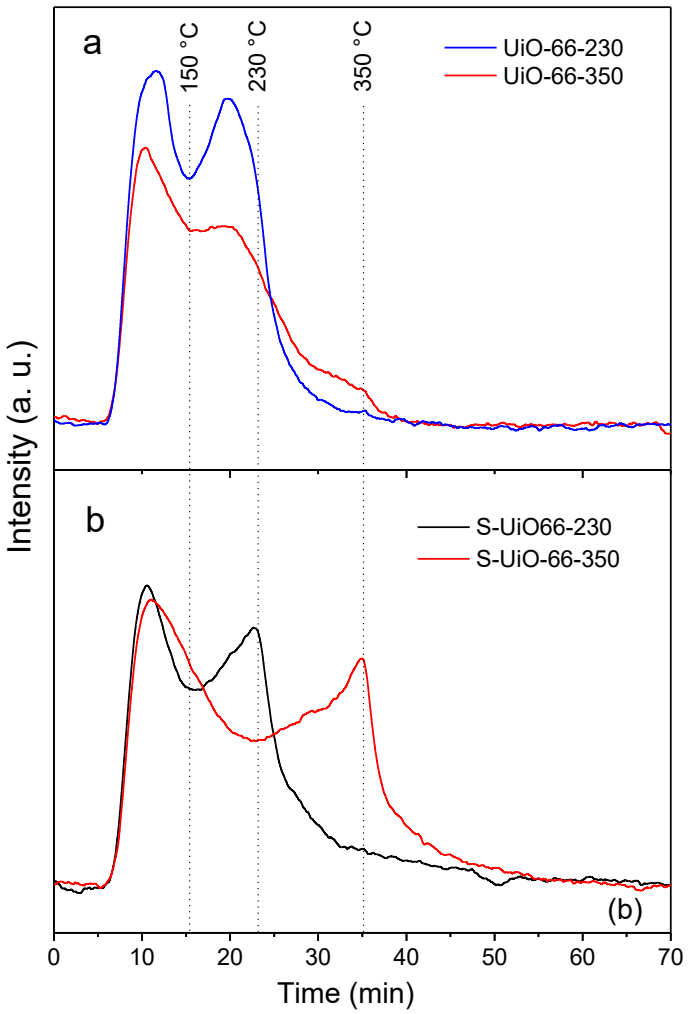

Figure S2. NH_3–TPD profiles: a) UiO–66 pretreated in He 60 min at 230 °C and 350 °C, respectively; b) sulfated UiO–66 pretreated in He 60 min at 230 °C and 350 °C, respectively.

Weak acid sites: obtained by integration of TPD area between 50 °C and 150 °C.
Medium acid sites: obtained by integration of TPD area between 150 °C and 230 °C.
Strong acid sites: obtained by integration of TPD area between 230 °C and 350 °C.

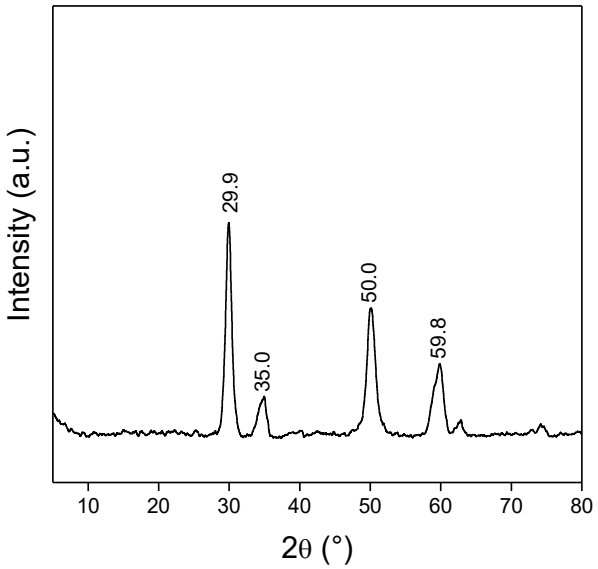

Figure S3. XRD of a thermally degraded UiO-66 sample, in which intense signals of tetragonal zirconia are observed.

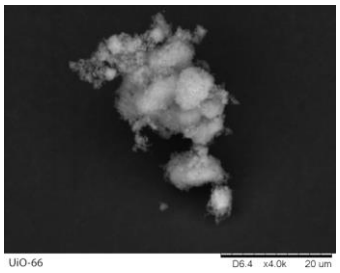

Sample	Atomic Zr/S*
Impregnated UiO-66	1.3
S-UiO-66-230	1.2
S-UiO-66-350	1.4

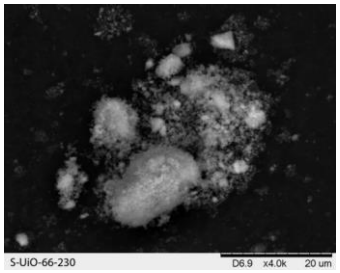

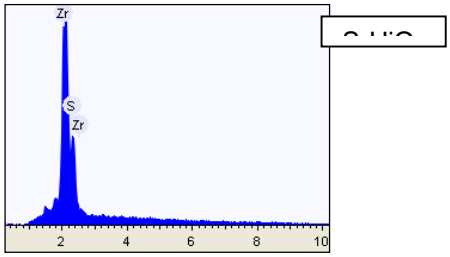

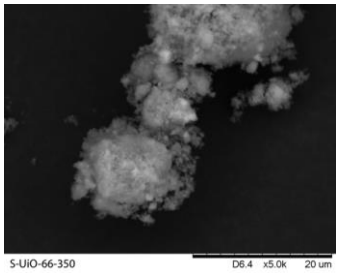

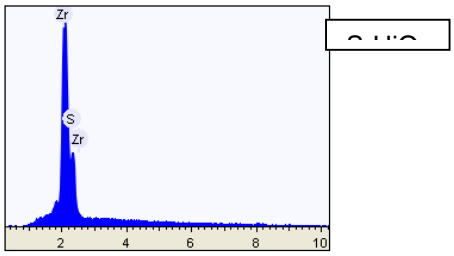

Figure S4. SEM images and EDS spectra of: a) Synthesized UiO-66; b) Sulfated UiO-66 treated at 230 °C in He for 60 min; c) Sulfated UiO-66 treated at 350 °C in He for 60 min; d) Table with the mean bulk atomic Zr/S proportions of sulfated samples.

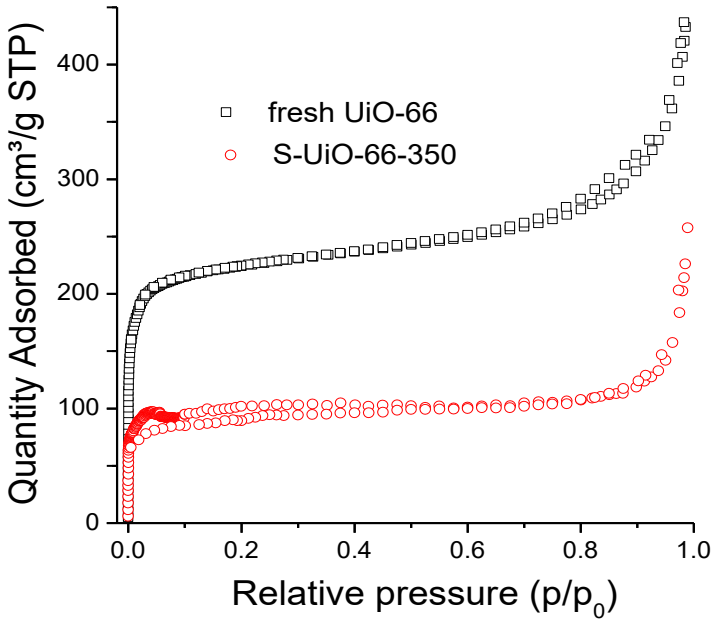

Figure S5. N_2 adsorption–desorption isotherms at 77 K.

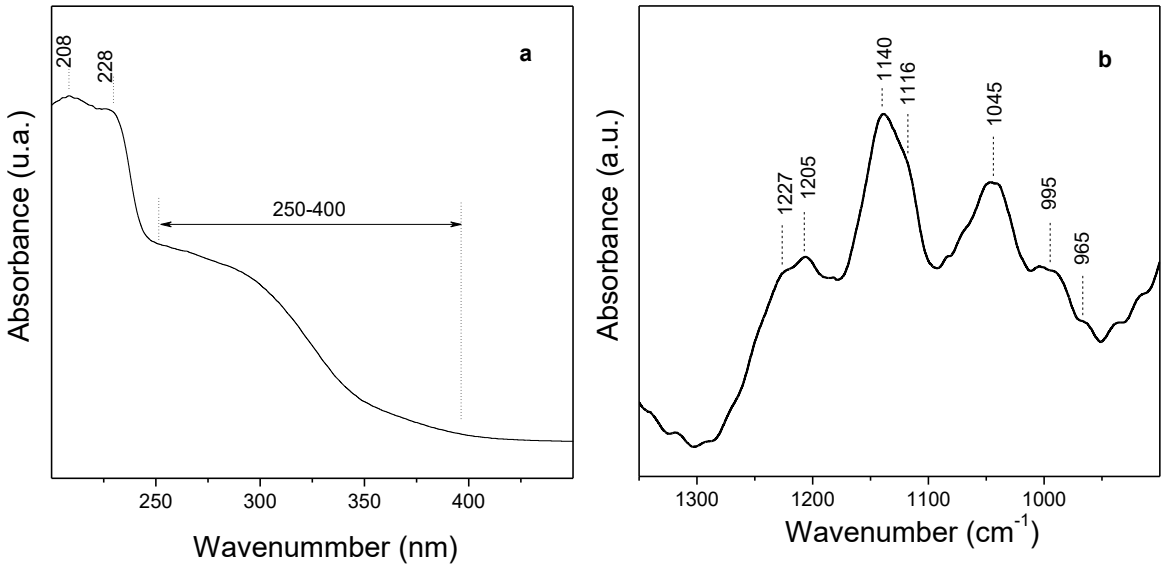

Figure S6. Sulfated zirconia sample prepared from commercial zirconium hydroxide (sulfate doped) MEL, grade XZ0682/01 which was treated by calcination 2 h in air at 500 °C. This sample was later analyzed for comparison in the isobutene dimerization (Figure S5.b): a) DRS UV–VIS spectra; b) FTIR spectra.

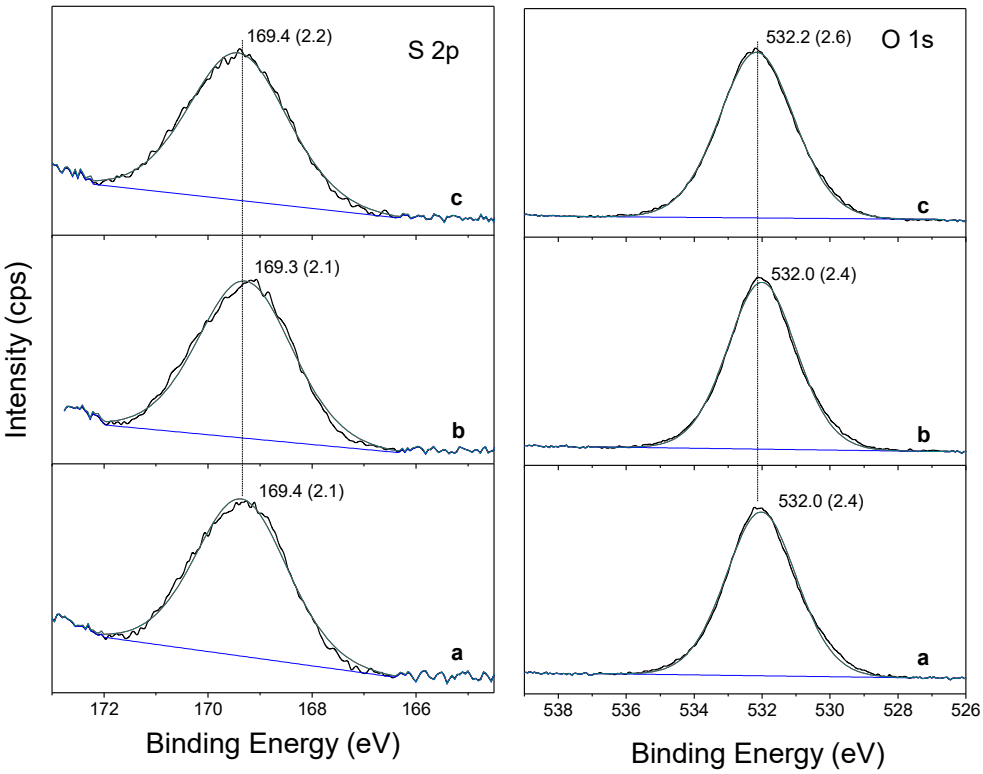

Figure S7. XPS spectra of sulfated MOF. Left S 2p region; Right O 1s region: a) impregnated UiO-66; b) S-UiO-66-230; c) S-UiO-66-350.

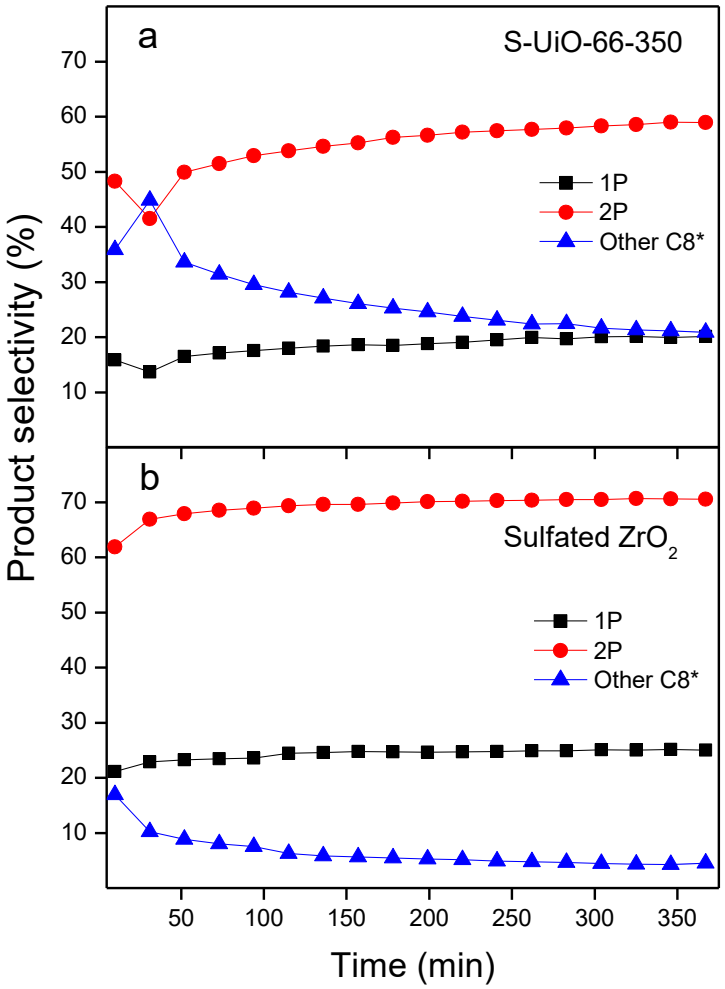

Figure S8. Selectivity of products in the isobutene dimerization reaction at 180 ° C for: a) S–UiO–66–350; b) commercial sulfated zirconia, where 1P refer to 2,4,4–trimethylpentene–1; 2P referes to 2,4,4–trimethylpentene–2. Other C8* products are probably 2,3,4–trimethylpentene–1, 2,3,4–trimethylpentene–2, 3,4,4– trimethylpentane–2(3,4,4–TMP–2) and others C8 as recently described by J. Liu, et al., Catal. Commun. 119 (2019) 57–61.